Three-dimensional phase field simulation of the effect of anisotropy in grain-boundary mobility on growth kinetics and morphology of grain structure

Yoshihiro Suwa [a,*], Yoshiyuki Saito [b], Hidehiro Onodera [c]

[a] *Computational Materials Science Center, National Institute for Materials Science, Sengen 1-2-1, Tsukuba, Ibaraki 305-0047, Japan*
[b] *Department of Materials Science and Engineering, Waseda University, Tokyo 169-8555, Japan*
[c] *Materials Engineering Laboratory, National Institute for Materials Science, Tsukuba 305-0047, Japan*

Abstract

The kinetics and topology of grain growth in three dimensions have been simulated using a phase-field model with anisotropic grain-boundary mobilities. In order to perform large scale calculations we have applied both modifications of algorithms and parallel coding techniques to Fan and Chen's phase-field algorithm. The kinetics of abnormal grain growth together with isotropic grain growth is presented. It is observed that the grains of a minor component which are at the beginning surrounded preferentially by boundaries with high mobility grow faster than the grains of a major component until the texture reverses completely. In our simulation program, data arrays for storing orientation field variables are divided into each message passing interface (MPI) domain, and only the information about the cluster enumeration is shared with whole system. This enables us to perform large scale calculations such as 320^3 grid points. In order to follow up the time-dependent growth exponent and distribution functions in a material with a strong texture, a large scale calculation is indispensable.
© 2006 Elsevier B.V. All rights reserved.

1. Introduction

The modelling of grain growth is essentially important for design of structural materials. Due to the difficulty of incorporating topological features into analytical theories of grain growth directly [1–6], there has been increasing interest in the use of computer simulations to study grain growth. A variety of models have been proposed [7,8] during the past decades, including Monte Carlo Potts models [9,10], vertex model [11,12], front tracking [13,14], Voronoi tessellation [15,16], cellular automata [17] and phase-field approaches [18–25]. All of these methods were originally applied to the 'ideal' case of coarsening of a polycrystalline in two dimensions (2D) solid with uniform grain-boundary mobilities and energies. For such a system, the various computational models reach similar conclusions regarding the kinetics and topological aspects of two dimensional grain growth, despite significant differences in underlying methodology [26,27].

The improvement of computing power in recent years, it has become possible to extend these 2D grain-growth simulations to 3D ones, which are necessary for a reasonable comparison with experimental data on bulk polycrystalline samples. The challenge here is the optimization of the computational algorithm which enables to treat a statistically significant number of grains under the limitation in computer power. This is usually a nontrivial task, because the memory and processing time in these

---
* Corresponding author. Tel./fax: +81 29 859 2610.
  E-mail address: SUWA.Yoshihiro@nims.go.jp (Y. Suwa).

simulations increase dramatically with the number of spatial dimensions. Until now, 3D systems containing more than 10^3 grains have been treated successfully using Monte Carlo Potts models [28–32], vertex model [33,34], Voronoi tessellation [35], cellular automata [36] and a boundary-tracking approach [37,38]. The phase-field method, however, is missing from the list, although it is considered to give the most versatile and mature approach for simulating coarsening phenomena, particularly in the presence of multiple phases or gradients of concentration, stress or temperature [26].

More recently, Krill and Chen [39] modified Fan and Chen's phase-field algorithm [20,21] to perform 3D simulations by applying the dynamic grain-orientation reassignment scheme. Kobayashi and Warren [40] extended their phase field model [23,24] to 3D. However, Krill and Chen's calculations were limited to an isotropic grain growth only. The total number of grains were limited in Kobayashi and Warren's calculations. The number of grains in their calculations was too small to obtain meaningful statistically significant results.

In this paper, we apply both modifications of algorithms and parallel coding techniques to Fan and Chen's phase field algorithm. We perform numerical simulations of grain growth in 3D by the phase field model with anisotropic grain-boundary mobilities. Computer simulations are performed on a simple cubic lattice with 320^3 grid points. Kinetics of abnormal grain growth together with isotropic grain growth is presented. Topological results of grain structures such grain size distributions, grain face distributions are also discussed.

2. Method

2.1. Phase field model

In the phase field model for the grain growth of polycrystalline materials [20,21], the microstructure of polycrystalline materials is described by a set of orientation field variables, $\eta_1(\mathbf{r},t), \eta_2(\mathbf{r},t),\ldots,\eta_Q(\mathbf{r},t)$, that distinguish different orientations of grains and are defined at a given time and each position $\mathbf{r}$ within the simulation cell; here Q is the number of possible orientations. Within a grain labeled by η_1, $\eta_1(\mathbf{r},t)$ equals 1 or −1, while all other field variables equal 0. At a grain boundary all $\eta_i(\mathbf{r},t)$ vary continuously between their equilibrium values in the neighbouring grains. According to Cahn's and Hilliard's treatment [41], the total free energy functional of an inhomogeneous system is given by

$$F = \int \left[f_0(\eta_1(\mathbf{r},t),\eta_2(\mathbf{r},t),\ldots,\eta_Q(\mathbf{r},t)) + \sum_{i=1}^{Q} \frac{\kappa_i}{2}(\nabla\eta_i(\mathbf{r},t))^2 \right] \mathrm{d}^3r$$
$$(i=1,2,\ldots,Q), \tag{1}$$

where f_0 is the local free energy density which is a function of orientation field variables, $\eta_i(\mathbf{r},t)$, and κ_i is the gradient energy coefficient. The spatial and temporal evolutions of the

orientation field variables are described by the time-dependent Ginzburg–Landau equations for nonconserved order parameter [42] as

$$\frac{\partial\eta_i(\mathbf{r},t)}{\partial t} = -L_i \frac{\delta F}{\delta\eta_i(\mathbf{r},t)} \quad (i=1,2,\ldots,Q), \tag{2}$$

where L_i are the Onsager's phenomenological coefficients. We used the Ginzburg–Landau type free energy density functional for the present simulation given by

$$f_0(\eta_1(\mathbf{r},t),\eta_2(\mathbf{r},t),\ldots,\eta_Q(\mathbf{r},t))$$
$$= \sum_{i=1}^{Q} \left(-\frac{a_1}{2}\eta_i^2 + \frac{a_2}{4}\eta_i^4 \right) + a_3 \sum_{i=1}^{Q}\sum_{j\neq i}^{Q} \eta_i^2\eta_j^2, \tag{3}$$

where a_1, a_2 and a_3 are phenomenological parameters. The only requirement for f_0 is that it has $2Q$ minima with equal well depth at $(\eta_1,\eta_2,\ldots,\eta_Q) = (1,0,\ldots,0),(0,1,\ldots,0),\ldots,$ $(0,0,\ldots,1),(-1,0,\ldots,0),(0,-1,\ldots,0),\ldots,(0,0,\ldots,-1)$. Therefore, a_3 has to be greater than $a_2/2$. In this paper, we set each order parameter equal to its absolute value, effectively restricting the available order parameter space to that containing only the Q degenerate minima of f_0 [43].

When L_i, κ_i and a_3 are assumed to be constant, the above equations describe isotropic grain growth. The mobility anisotropy is incorporated by making L_i dependent on the misorientation [44]. And the energy anisotropy can be introduced by making κ_i and a_3 dependent on the misorientation under the constraint of the constant grain boundary width [44,45]. According to Ma et al. [44], we characterize the misorientation field corresponding to an arbitrary distribution for grain boundary in the system as

$$\theta(\mathbf{r},\mathbf{t}) = \frac{\sum_{i,j\neq i}^{Q}\eta_i(\mathbf{r},t)^2\eta_j(\mathbf{r},t)^2\theta_{ij}}{\sum_{i,j\neq i}^{Q}\eta_i(\mathbf{r},t)^2\eta_j(\mathbf{r},t)^2}, \tag{4}$$

where θ_{ij} is the misorientation angle between grain i and grain j with orientations η_i and η_j, respectively. Eq. (4) assigns a constant misorientation angle within the grain-boundary region between grain i and grain j with the value of θ_{ij}, given by a predetermined look-up table, and yield a weighed-mean misorientation at junction.

For the purpose of simulating the grain growth kinetics, the set of kinetic equation (2) have to be solved numerically by discretizing them in space and time. The Laplacian is discretized by the following equation:

$$\nabla^2\eta_i(\mathbf{r},t) = \frac{1}{(\Delta x)^2}\sum_j(\eta_j(\mathbf{r},t)-\eta_i(\mathbf{r},t)), \tag{5}$$

where Δx is the discretizing grid size, j represents the first nearest neighbours of site i. For discretization with respect to time, we used the simple explicit Euler equation,

$$\eta_i(\mathbf{r},t+\Delta t) = \eta_i(\mathbf{r},t) + \frac{\partial\eta_i(\mathbf{r},t)}{\partial t}\times\Delta t, \tag{6}$$

where Δt is the time step for integration.

2.2. Dynamic grain-orientation reassignment

Krill and Chen [39] modified Fan and Chen's phase-field algorithm in order to perform 3D simulations by applying the dynamic grain-orientation reassignment scheme. Because the orientations of individual grains can be reassigned without affecting the underlying physics of coarsening, it is possible to avoid the coalescence of neighbouring grains by the scheme. In this manner, model-independent results were obtained with Q as small as 20, permitting large-scale simulations for the first time in 3D using the phase field approach.

In this paper, we extend their scheme to an anisotropic system. In their approach, dynamic grain-orientation reassignment was performed after each time step with the exclusive focus on the elimination of matches in grain-orientation between first-nearest-neighbour grains. However, this procedure is not suitable for parallel coding technique. Therefore, we modified their approach as follows:

- All orientation variables are divided into groups of orientation. Orientations belonging to the same group are assumed to have the same grain-boundary properties. In other words, if orientation i and j belong to the same group, we assumed that $\theta_{iq} = \theta_{jq}$, $\theta_{qi} = \theta_{qj}$ ($q = 1, 2, \ldots, Q$). Additionally, $\theta_{qq} \neq 0$ ($q = 1, 2, \ldots, Q$) is also assumed, where θ_{ij} is the misorientation angle between grain i and grain j with orientations η_i and η_j.
- A list of the order parameter indices of the nearest and next-nearest grains to each grain present in the simulation cell is maintained throughout a simulation.
- At a particular time step, each grain is checked by a cluster enumeration technique [46] for a match between its orientation and those in the list: if a match is found the order-parameter values of the given grain are reassigned to a new one not present in the list. Note, however, that the new one has to belong to the same group as the older one.

Krill and Chen pointed out [39] that approximately 50 order parameters would be needed to implement above scheme in 3D even in the isotropic system. In our simulations, approximately 60 order parameters were needed because we adopted Voronoi tessellation as initial structures. In order to reduce the total number of orientation field variable, we define distances between grains that are next-nearest-neighbour to each other. And if the distances are large enough, we do not need to take into account the orientations of the grains in the matching events. Schematic illustration of the definition of the distance d_{ij} (TYPE-A) is shown in Fig. 1a. This distance is defined as follows:

- The center of each grain is defined by the maximum and minimum value along each axis.
- The size of a grain in the simulation cell is determined by counting the lattice points located within the boundaries
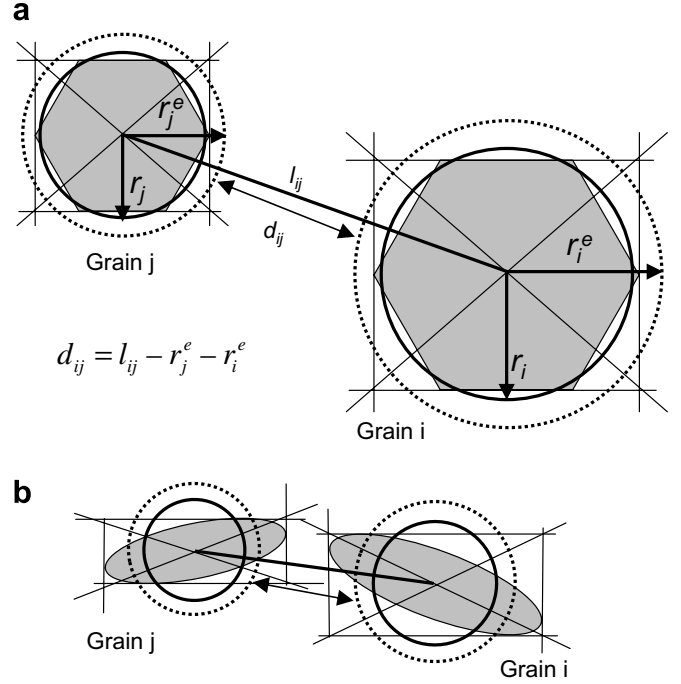
$$d_{ij} = l_{ij} - r_j^e - r_i^e$$

Fig. 1. (a) Schematic illustration of the definition of the distance, d_{ij}, between grain i and j. Grain radius, r_i, is measured by the cluster enumeration technique. (b) The distance, d_{ij}, has a possibility to over estimate the distance between grains with high aspect ratio.

of the grains, V_i, and then defining, r_i to be the radius of a sphere of equivalent volume.
- Then, d_{ij} between grains i and j is defined as $d_{ij} = l_{ij} - r_i^e - r_j^e$, where l_{ij} is the distance in a straight line between the center of grains i and j, and r_i^e and r_j^e are the effective radius of grain i and j, respectively. r_i^e and r_j^e are introduced to take into account the exact geometry of grains. In this study, r_i^e ($i = 1, 2, \ldots,$ number of grains) are assumed to be $1.2 r_i$.

However, the distance, d_{ij} has a possibility to overestimate the distance between grains with high aspect ratio. (see Fig. 1b) Then, we also defined another distance, D_{ij} (TYPE-B). Schematic illustration of the definition of D_{ij} is also shown in Fig. 2. This distance is defined as follows:

- The distances between grains i and j along each axis are defined as D_{ij}^k ($k = x, y, z$).
- Then, we define the distance D_{ij} between grains i and j is defined as $D_{ij} = ((D_{ij}^x)^2 + (D_{ij}^y)^2 + (D_{ij}^z)^2)^{1/2}$.

D_{ij} and d_{ij} are calculated on the lattice systems with periodic boundary condition. By introducing these distances simultaneously, the total number of order parameters needed in isotropic system is reduced to 30. Although we are not able to assign a unique orientation to each grain, at least 12 different texture components can be handled simultaneously with 80 order parameters by implementing the dynamic grain-orientation reassignment (Because of
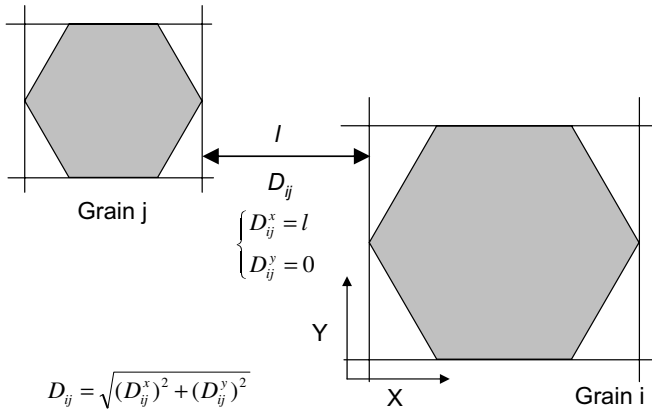
Fig. 2. Schematic illustration of the definition of the distance, D_{ij}, between grain i and j.

the limitation in memory resources, we could not perform a simulation with over 80 order parameters.).

At the beginning of a simulation, it is difficult to estimate the total number of order parameters needed throughout the simulation. Therefore, we apply a dynamic grain-orientation addition scheme. In the dynamic grain-orientation reassignment, if we has no available orientation in the same group, G_i, we add one orientation to the total number of order parameters. Then, the $(Q + 1)$th order parameter becomes a new member of the group G_i.

The program flowchart is shown in Fig. 3. Both the message passing interface (MPI) and an automatic parallelization scheme of the FORTRAN compiler are implemented to calculate the series of Eq. (2). Only the MPI is implemented to perform the cluster enumeration scheme. In our simulation program, data arrays for storing orientation field variables are divided into each MPI domain, and only the information about the cluster enumeration is shared

with whole system. It is quite easy to solve the series of Eq. (2) numerically with explicit finite difference method. The only requirement is that the data arrays locate along the surfaces of each adjacent MPI domain has to communicate each other at every time step. Compared to the parallelization of solving series of Eq. (2), that of the cluster enumeration is rather complex. In the cluster enumeration scheme, the most time consumable part is to check the connectivity of each cluster i.e. each grain. Because, this part requires huge amount of iterative analyses and is not compatible to the parallelization technique due to the structure of the algorithm. Therefore, we divide this connectivity check into two parts. One part is the connectivity check in each MPI domain, and the other part is the connectivity check between grains faced each other via the surfaces between each MPI domain. In order to take into account the existence of a large grain shared by more than 2 MPI domains, the latter part has to be repeated a few times. By utilizing this connectivity check algorithm, elapsed time is reduced to 1/8 of the old algorithm. (Eight MPI processes are involved in our calculation.)

3. Results and discussion

3.1. Isotropic grain growth

Hereafter, the parameters, length, area and volume are expressed in number of grid points (g.p.) and time in the dimensionless time (s'). Simulations are performed on 3D lattice with size of 320^3(g.p.) and the total number of orientations of $Q = 30$. Dynamic grain-orientation reassignment and addition are performed with prescribed time interval of $t_i = 25$, 50 and 100 steps depending on the averaged grain radius, $\langle R \rangle(t)$. In the case of isotropic-boundary system, the possibility of coalescence is positively correlated with the growth rate. Therefore, t_i is assigned to be inversely proportional to $\langle R \rangle(t)$. On the other hand, the threshold value for the distances, d_{ij} and D_{ij} is assigned to be proportional to $\langle R \rangle(t)$. At the end of simulations, Q increases to 31 or 32 by dynamic grain-orientation addition. The lattice step size Δx is set to be 1.0 and a time step Δt of 0.05 is employed. The coefficients appearing in Eqs. (1)–(3) are chosen to have the values $a_1 = a_2 = a_3 = 1$, $\{\kappa_i\} = 2.0$ and $\{L_i\} = 1.0$ for $i = 1$ to Q. All simulations are performed on the lattice systems with periodic boundary condition. In order to prevent large discontinuous change in grain size by coarsening of grains having the same orientation at initial stage, the nucleation sites are set so that grains with same orientation locate at distance of a preset minimum distance in each phase field. This initial structure is equivalent to that of weighted Voronoi tessellation (which divides the volume into cells, each of which contains all points closer to one of a set of predefined points than any other such point) [47]. The total numbers of nucleation sites are 17,580 (586×30). To visualize the microstructure evolution using the orientation field variables, the following function was defined:
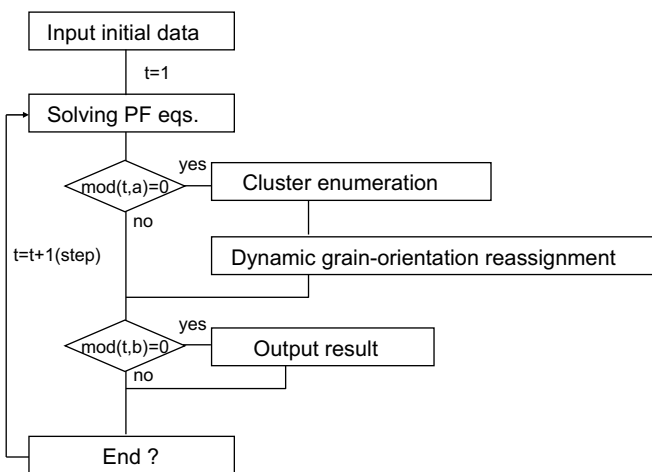

Fig. 3. Program flowchart of our simulation code, where a and b are a prescribed time interval for a cluster enumeration and a data output, respectively. And "mod(t, a) = 0" means "If the current time step is dividable by the prescribed time interval, a, ...". The values of 25, 50 and 100 were used for "a" and the value of 400 was used for "b".

$$\varphi(\mathbf{r}, t) = \sum_{i=1}^{Q} \eta_i^2(\mathbf{r}, t), \qquad (7)$$

which takes a value of unity within individual grains and smaller values in the core regions of the boundaries [20,21]. If we map the value of $\varphi(\mathbf{r}, t)$ to a spectrum of graylevels, then we obtain images like that of Fig. 4, in which the grain boundaries appears as dark regions separating individual grains. In order to get statistical values such as grain size and grain face distributions, three runs of simulation are performed. All calculations in this paper are performed on the Numerical Materials Simulator (HITACHI SR11000) at National Institute for Materials Science (NIMS) with 2 nodes (number of central processing units: $16 \times 2 = 32$, memory for application codes: $24 \times 2 = 48$ GB). Isotropic simulation represents about 18 h of computing time for 20,000 steps ($1000s'$).

According to analytic theories for normal grain growth [1,3], following an initial transient of duration t_0, the average grain radius $\langle R \rangle$ is expected to increase with time t as $\langle R \rangle^2(t) = \langle R \rangle^2(t_0) + k(t - t_0)$, where $\langle R \rangle(t_0)$ denotes the average grain radius at t_0, and k is a constant related to the grain-boundary mobility. The size of a grain in the simulation cell is determined by counting the lattice points located within the boundaries of the grain, multiplying by $(\Delta x)^3$ to obtain the grain volume V, and then defining R_V to be the radius of a sphere of equivalent volume: $R_V = (3V/4\pi)^{1/3}$ (Before determining the individual grain volumes, all lattice points located within the grain boundary regions are assigned to the nearest grain.). Averaging over all of the grain present in the cell, we obtained the time evolution of $\langle R_V \rangle$ plotted in Fig. 5.
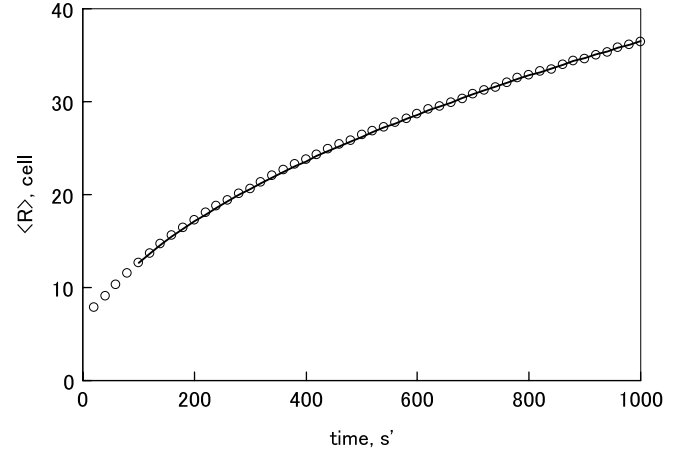

Fig. 5. Temporal evolution of the average grain radius $\langle R \rangle$ in phase-field simulation in isotropic case (open circles). Solid curve is the result of a nonlinear least squares fit of Eq. (8) over the time interval $100.0 < t < 1000.0 (s')$.

$$\langle R \rangle^m(t) = \langle R \rangle^m(t_0) + k(t - t_0), \qquad (8)$$

where m, $\langle R \rangle(t_0)$ and k are fitting parameters. By performing a nonlinear least-squares fitting to the data of Fig. 5 for $t \geqslant t_0 = 100.0 s'$, we have obtained the value of 2.05 for the growth exponent. The obtained value of 2.05 agrees well with the theoretical prediction and with computer simulations carried out in 2D [7,9,20,48,49] as well as 3D [28–47].

The scaled grain size distribution is shown in Fig. 6. The steady state distribution predicted by Hillert [4] is plotted for comparison. After a short transient time, the grain size distribution becomes time-independent. Simulated grain
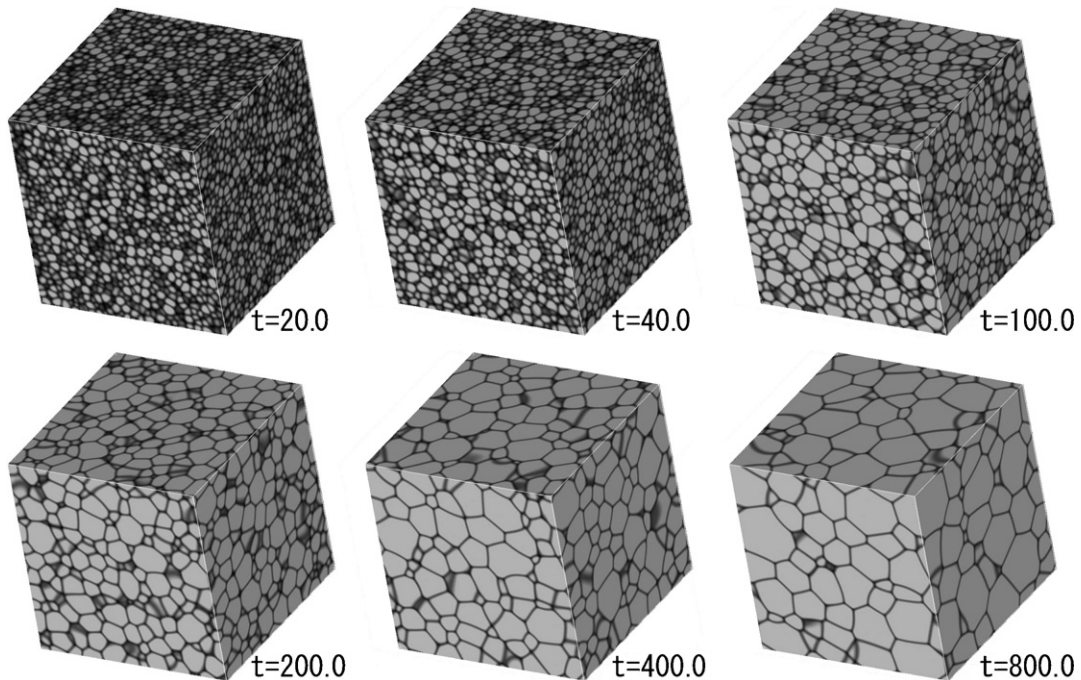

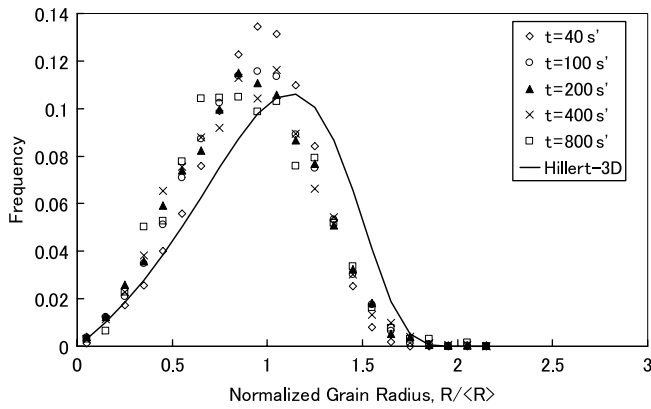Fig. 4. Simulated microstructural evolution in 320^3 cells in isotropic case.

Fig. 6. Variation in the scaled grain size distribution function with time in isotropic case. The data points were averaged over the results of three separate runs at the indicated times. For comparison, the steady-state distribution predicted by Hillert theory [4] is plotted as the solid curve.

Fig. 8. Relation between the average number of faces of neighbor of N-face grain, $m(N_f)$ and the face number, N_f in isotropic case. The data points were averaged over the results of three separate runs at $t = 300s'$. Solid curve is the results of a least-squares fit of data points in the range of $4 < N_f < 30$.

size distribution functions are slightly narrower than those obtained in Krill and Chen's works. This is attributed to two reasons. One is the difference in the initial size-distribution functions. According to Nagai et al. [50], the relaxation process of the size distribution function is slower than that of the average grain size. Therefore, the difference in the initial structure remain for a long period. Another is the width of grain boundaries in relation to the width of a grid size. As the small grains in phase field representation shrink, they approach the resolution limit of the grain boundary region and "disappear" prematurely [26]. Then, the width of grain boundary affects on the disappearance of grains and distribution functions.

The distributions of the number of face, N_f, for individual grains of the simulated microstructures is shown in Fig. 7. The distribution becomes time-invariant at the longer time. The frequency increase rapidly for a small number of faces and peaks at a value of 12–14 and decays quickly. Simulated face distribution functions are also slightly narrower than those obtained in Krill and Chen's works. In our simulation, the initial value of the average number of faces per grain, $\langle N_f \rangle$ was 15.0. After a short transient time, the value approached to a constant value

of about 13.7, which is in good agreement with that obtained by the previous investigations [39,47].

The relationship between the average number of faces of per grain adjacent to an N-faced grain, $m(N_f)$, and the face number in grains, N_f, is shown in Fig. 8. The linear relation similar to the Aboav–Weaire relations [51,52] is obtained between $m(n)$ and N_f as

$$m(N_f) \times N_f = 13.6N_f + 27.2. \tag{9}$$

3.2. Effect of anisotropy in grain-boundary mobility

The texture development during grain growth has been studied mainly through statistical modelling [53–56] and Monte Carlo simulations [57–66]. Abbruzzese et al. [53,54] studied interactions between two texture components by extending Hillert's statistical model [4] of grain growth. For simplicity, they considered two types of grain orientation (or texture components) A and B with three types of grain boundaries (A–A, B–B and A–B). Accounting for anisotropy only in boundary mobility, with high mobility for A–B and low mobility for A–A and B–B boundaries, they have shown that the minority component should grow at the expense of the majority component, leading to oscillations in the volume fractions of the two texture components. Such a phenomenon has been observed in the Monte Carlo simulations by Mehnert and Klimanek [61,62] and Ivasishin et al. [63].

In order to compare with their results, we also consider two types of texture components A and B. And, we examine only the effects of the grain-boundary mobility anisotropy, with high mobility for A–B and low mobility for A–A and B–B boundaries. In general, the grain-boundary energy has to be defined as a function of the misorientation as well as the grain-boundary mobility. However, the decrease in the energy is negligibly small compared to that in the mobility, provided that the misorientation between grains with the same texture component is not so small [56]. In this study, we assumes this situation.
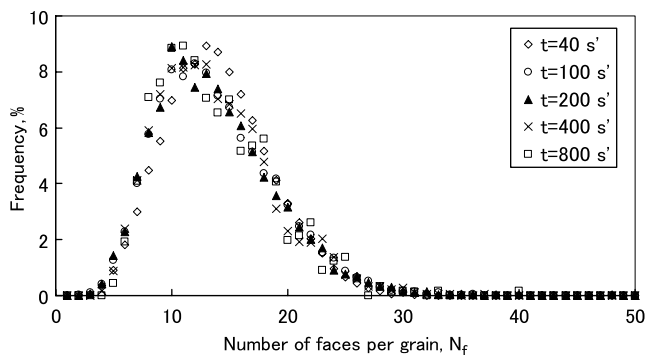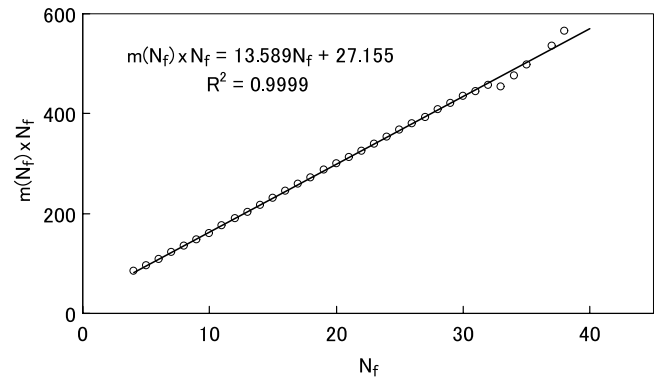

Fig. 7. Variation in the face number distribution function with time in isotropic case. The data points were averaged over the results of three separate runs at the indicated times.

The effects of the volume fraction ratio of textures in the initial structures, f_a^0/f_b^0 on the grain growth kinetics are analyzed, where f_a^0 and f_b^0 represent the initial volume fraction of grains belonging to component A and component B, respectively. Simulation are performed on 3D lattice with size of 320^3 (g.p.) and the number of orientations of $Q = 30$. Dynamic grain-orientation reassignment and addition are performed with prescribed time interval of $t_i = 25$, 50 and 100 steps depending on the averaged grain radius, $\langle R \rangle(t)$. In anisotropic systems, the possibility of coalescence has to be considered between grains with the same texture component only. The boundaries between grains with the same texture component have small mobility. Therefore, we have to focus especially on the possibility of the coalescence between abnormally grown B grains. Because large grains have large effective radius and the mobility anisotropy is not so strong, the time intervals, which are employed in the isotropic cases, are short enough for the anisotropic cases. At the end of simulations, Q have increased to 49 or 50 by dynamic grain-orientation addition. The lattice step size Δx is set to be 1.0 and a time step Δt of 0.05 is employed. The total numbers of nucleation

sites are 17,580 (586×30). The coefficients appearing in Eqs. (1)–(3) are chosen to have the values; $a_1 = a_2 = a_3 = 1$, $\{\kappa_i\} = 2.0$ for $i = 1$ to Q. The mobility anisotropy is characterized by

$$L(\theta) = \begin{cases} 0.2 & \text{(between grains of the same texture component)}, \\ 1.0 & \text{(between grains of different texture component)}. \end{cases}$$
(10)

An initial polycrystalline microstructure is created by simulating normal grain growth for 1000 steps ($50s'$). This structure is then divided into two components by means of an appropriate critical orientation number, q_c.

3.2.1. Case 1 (Initial fractions of $f_a^0 = 0.8$ and $f_b^0 = 0.2$)

In order to generate microstructures with volume fractions of $f_a^0 = 0.8$ and $f_b^0 = 0.2$, the critical orientation value is set to 24 such that all orientations $1 \leqslant q \leqslant 24$ belongs to the component A and all $25 \leqslant q \leqslant 30$ to the component B, respectively.

Fig. 9 depicts temporal evolution of microstructure with $f_a^0 = 0.8$ and $f_b^0 = 0.2$. In the microstructures, grains
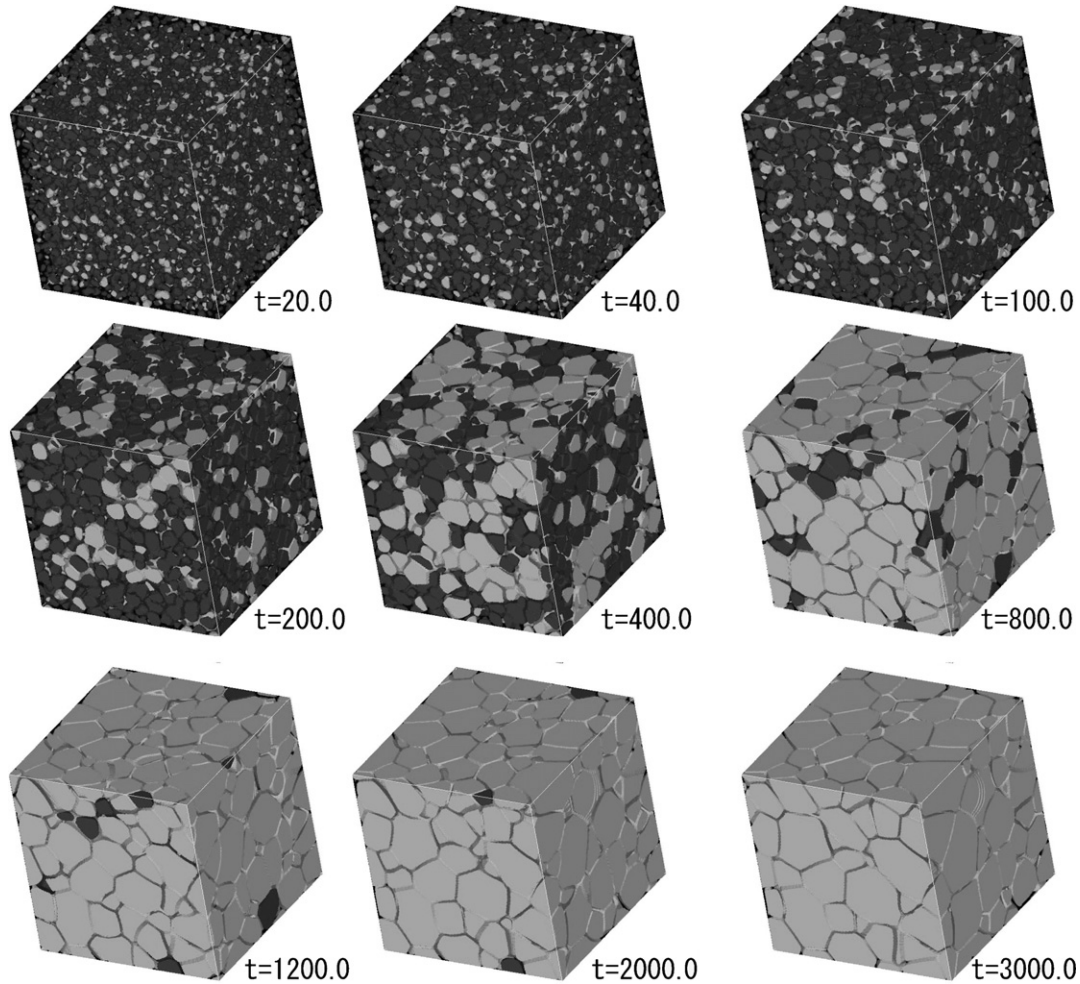

Fig. 9. Simulated microstructural evolution in 320^3 cells with two texture component A (dark gray) and B (light gray) of different initial volume fraction ($f_A^0 = 0.8, f_B^0 = 0.2$) and a mobility ratio of 0.2.

belonging to the component A are darkly shaded while grains belonging to component B are lightly shaded. This simulation represents about 140 h of computing time for 80,000 steps ($4000s'$). Due to huge computation time, only one simulation is performed. However, except for the late stage ($t > 1000s'$), obtained distribution functions are smooth enough for discussion.

The temporal evolutions of average radius for grains of the component A, the component B and both components, $\langle R_A \rangle$, $\langle R_B \rangle$ and $\langle R \rangle$ are shown in Fig. 10. In this figure, the growth kinetics of $\langle R \rangle$ can be divided into three different stages. In order to obtain a value for the growth exponent m at each stage, we perform a nonlinear least-squares fit to the data of Fig. 10. At the end of the simulation, the whole microstructure contained only one grain of the component A.

The growth process simulated here exhibits the general characteristics of grain growth in a material with strong textures [62]:

- At the beginning the grains of component B are mainly surrounded by grains of component A. For this reason, the boundaries of the grains of component B are merely high angle boundaries with a high mobility. This leads to a preferred growth of component B.
- The accelerated growth of component B lasts until its grains impinge each other forming low angle boundaries.
- At the beginning, the grain growth exponent, m of $\langle R \rangle$ is clearly higher than $m = 2.0$. During the texture change m decreases drastically ($m < 2$). When the change is completed the exponent is in the same range at the beginning.

The grain size distribution for grains of the component A and the component B and both components normalized in $\langle R \rangle$ is shown in Fig. 11. In the isotropic system, the grain size distribution becomes time-independent after a short transient time as shown in Fig. 6. In this system, however, the grain size distributions exhibit time-dependent nature. The time dependence of distribution functions shows also
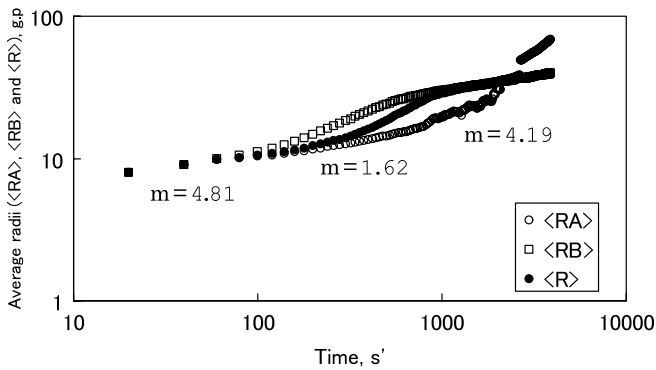

Fig. 10. Temporal evolution of the average grain radii ($\langle R_A \rangle$, $\langle R_B \rangle$ and $\langle R \rangle$) in a simulation with two texture component A and B of different initial volume fraction ($f_A^0 = 0.8, f_B^0 = 0.2$) and a mobility ratio of 0.2. The grain growth exponents, m, at various stage are described in the figure.
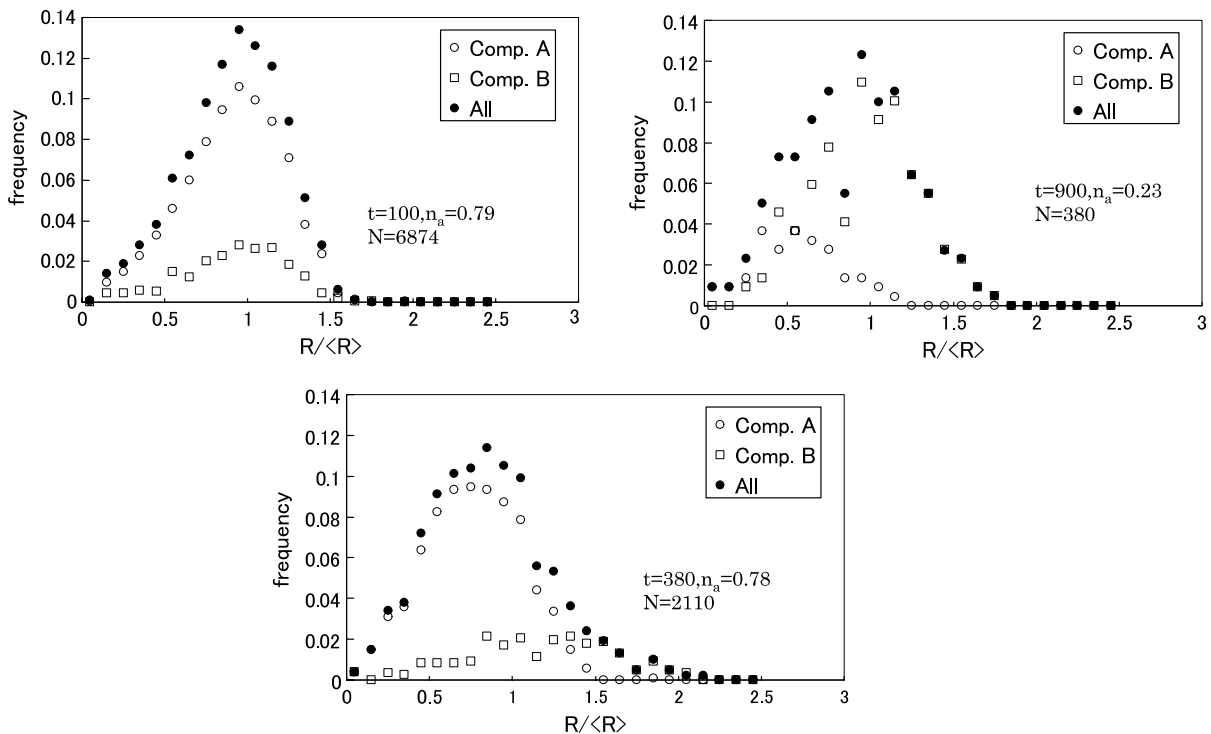

Fig. 11. Variation in the scaled grain size distribution function at different time step in a simulation with two texture component A and B of different initial volume fraction ($f_A^0 = 0.8, f_B^0 = 0.2$) and a mobility ratio of 0.2. The quantity N and n_a specify the total number of grains and the number fraction n_a of component A in the simulation cell, respectively.

general characteristics of grain growth in a material with a strong texture. This phenomenon was observed by Eichelkraut et al. [54] in their statistical simulations.

3.2.2. Case 2 (Initial fractions of $f_a^0 = 0.97$ and $f_b^0 = 0.03$)

According to Eichelkraut et al. [54], the grain growth in a material with a strong texture is characterized by the prominent increase of the ratio f_a^0/f_b^0. Therefore, we perform simulations with $f_a^0 = 0.97$ and $f_b^0 = 0.03$. In order to generate microstructures with volume fractions of $f_a^0 = 0.97$ and $f_b^0 = 0.03$, the critical orientation value is set to 29 such that all orientations $1 \leqslant q \leqslant 29$ belongs to the component A and only $q = 30$ to the component B. Fig. 12 depicts temporal evolution of microstructure with $f_a^0 = 0.97$ and $f_b^0 = 0.03$. In the microstructures, grains belonging to the component A are darkly shaded while grains belonging to the component B are lightly shaded. In order to get statistical values such as grain size and grain face distributions, three runs of simulation are performed. These simulations need about 50 h of computing time for 28,000 steps ($1400s'$) for each run. At the beginning of third stage, the calculations are terminated because grains of the component A completely disappear.

The temporal evolutions of average radius for grains of the component A, the component B and both components, $\langle R_A \rangle$, $\langle R_B \rangle$ and $\langle R \rangle$ are shown in Fig. 13. In this figure, the growth of $\langle R \rangle$ can be also divided into three different stages. Because simulations have been terminated at the beginning of the third stage, we have obtained variations in a value for the growth exponent m at the first and the
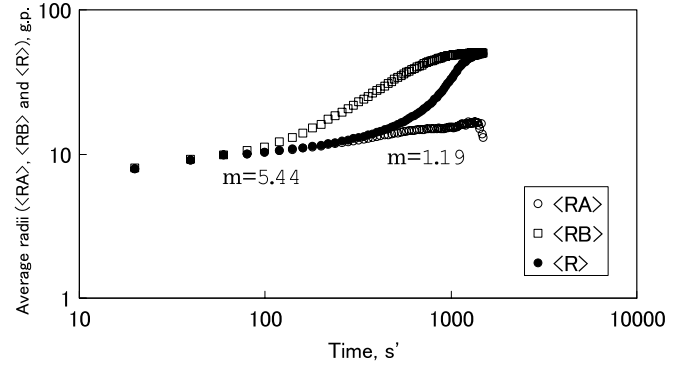

Fig. 13. Temporal evolution of the average grain radii ($\langle R_A \rangle$, $\langle R_B \rangle$ and $\langle R \rangle$) in a simulation with two texture component A and B of different initial volume fraction ($f_A^0 = 0.97$, $f_B^0 = 0.03$) and a mobility ratio of 0.2. The data points were averaged over the results of three separate runs at the indicated times. The grain growth exponents, m, at various stage are described in the figure.

second stages only. Compared with those obtained in the case of $f_a^0 = 0.8$ and $f_b^0 = 0.2$, the growth exponent, m at the first stage becomes larger and the growth exponent at the second stage becomes smaller. Due to the smaller number of grains of the component B, they could grow to larger sizes until the impingement occurs.

The grain size distribution for grains of the component A, the component B and both components normalized in $\langle R \rangle$ is shown in Fig. 14. In the case of $f_a^0 = 0.8$ and $f_b^0 = 0.2$, the distributions exhibit time-dependent nature but their peaks do not bifurcate. In contrast, we observe the bifurcation in the peak of the distribution function, $\langle R \rangle$ with $f_a^0 = 0.97$ and $f_b^0 = 0.03$ especially at $t = 1000s'$.
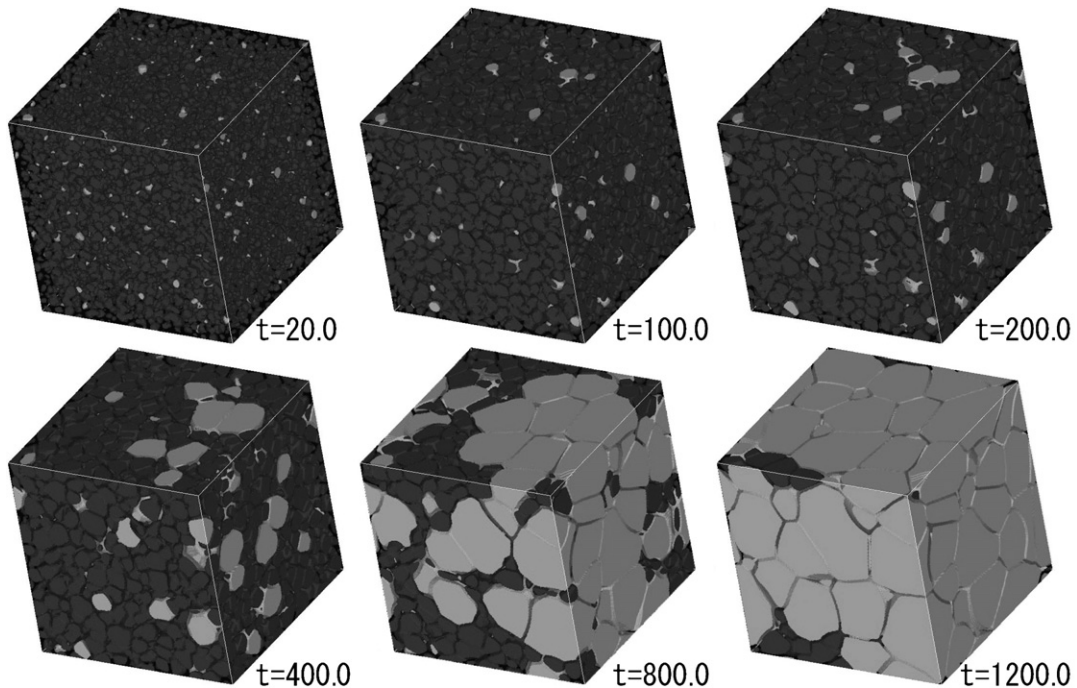

Fig. 12. Simulated microstructural evolution in 320^3 cells with two texture component A and B of different initial volume fraction ($f_A^0 = 0.97$, $f_B^0 = 0.03$) and a mobility ratio of 0.2.
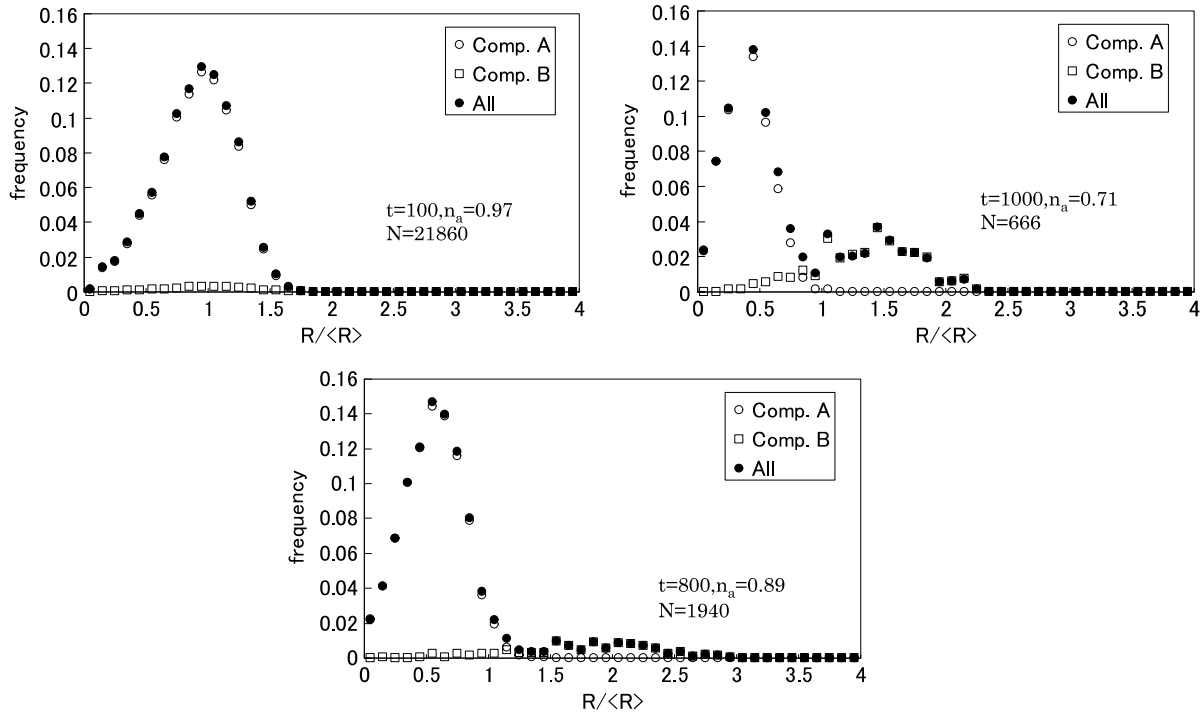
Fig. 14. Variation in the scaled grain size distribution function at different time step in a simulation with two texture component A and B of different initial volume fraction ($f_A^0 = 0.97, f_B^0 = 0.03$) and a mobility ratio of 0.2. The data points were averaged over the results of three separate runs at the indicated times. The quantity N and n_a specify the total number of grains and the number fraction n_a of component A in the simulation cell, respectively. N was obtained by combining the results of three separate simulation runs at the indicated times.

Furthermore, in the second stage, grains of the component B with more than 60 neighbouring grains are observed. This is not observed in the isotropic grain growth.

4. Concluding remark

In this paper, we have applied both modifications of algorithms and parallel coding techniques to Fan and Chen's phase field algorithm for grain growth in order to improve computational efficiency. For evaluations of the new algorithms, we have performed numerical simulations of grain growth in 3D with isotropic grain boundary properties. We have obtained a value for the growth exponent m of 2.05 which agrees with the theoretical prediction and with computer simulations carried out in 2D as well as 3D. Predicted size and face distribution functions are in good agreement with computer simulations carried out in 3D. And the topological correlations on the shapes of neighbouring grains, the Aboav–Weaire type law in 3D has been observed.

Next, we have applied the new algorithms to numerical simulation with anisotropic grain boundary mobilities. We have considered two types of texture components A and B. And we have examined the effects of the anisotropy in the boundary mobility, with the high mobility for A–B and the low mobility for A–A and B–B boundaries. The effects of volume fraction ratio of textures in the initial structures, f_a^0/f_b^0 on the grain growth kinetics have been analyzed. We have confirmed that the characteristics of grain growth

in a material with a strong texture become prominent with the increase of the ratio f_a^0/f_b^0.

We have performed numerical simulation with the initial structures of $f_a^0 : f_b^0 = 29 : 1$. In this case, only one orientation variable is assigned to the minor component B. Therefore, when the grains impinge each other, a huge amount of coalescence of grains could have been observed without the dynamic grain-orientation reassignment. This sequence of coalescence has the possibility to exert a great influence on the grain growth kinetics. In order to compare with pervious results, two types of texture components and the grain-boundary mobility anisotropy have been only taken into account. However, our simulation code has possibility to handle at least 12 different texture components simultaneously with considering the mobility and the energy anisotropy. And the simulation code has been successfully applied to a system containing finely dispersed second-phase particles [67].

The computation time for the dynamic grain-orientation reassignment is at most 10% of the total computation time. In the simulation code, data arrays for storing orientation field variables are divided into each MPI domain, and only the information about the cluster enumeration is shared with whole system. This enables us to perform large scale calculations such as 320^3 grid points. As mentioned above, the growth exponent and the distribution functions are time-dependent in a material with a strong texture. In order to follow up these quantities, a large scale calculation is indispensable.

Because numerical simulations with grain-boundary mobility anisotropy by the phase field or Monte Carlo method require huge computer resources especially in 3D, statistical modelling based on the mean field approach is still most practical at the present time. However, local alignment of grains and grain boundaries play a critical role when we take into account the dispersions of the texture component [44] or perform numerical simulations of the nucleation of recrystallization by abnormal subgrain growth mechanism [68–70]. In these cases, it is indispensable to apply direct simulations such as Monte Carlo, phase field and vertex simulation.

References

[1] H.V. Atkinson, Acta Metall. 36 (1988) 401–469.
[2] D. Weaire, J.A. Glazier, Mater. Sci. Forum 94–96 (1992) 27–38.
[3] F.J. Humphreys, M. Hatherly, Recrystallization and related annealing phenomena, Pergamon Press, Oxford, 1996 [Chapter 9].
[4] M. Hillert, Acta Metall. 13 (1965) 227–238.
[5] J.E. Burke, D. Turnbull, Prog. Metal. Phys. 3 (1952) 220–292.
[6] N.P. Louat, Acta Metall. 22 (1974) 721–724.
[7] H.J. Frost, C.V. Thompson, Curr. Opin. Solid State Mater. Sci. 1 (1996) 361–368.
[8] C.V. Thompson, Solid State Phys. 55 (2001) 269–314.
[9] M.P. Anderson, D.J. Srolovitz, G.S. Grest, P.S. Sahni, Acta Metall. 32 (1984) 783–791.
[10] D.J. Srolovitz, M.P. Anderson, P.S. Sahni, G.S. Grest, Acta Metall. 32 (1984) 793–802.
[11] K. Kawasaki, T. Nagai, K. Nakashima, Phil. Mag. B 60 (1989) 399–421.
[12] D. Weygand, Y. Bréchet, J. Lépinoux, Phil. Mag. B 78 (1998) 329–352.
[13] H.J. Frost, C.V. Thompson, C.L. Howe, J. Whang, Scr. Metal Mater. 22 (1988) 65–70.
[14] K. Marthinsen, O. Hunderi, N. Ryum, in: L.-Q. Chen, B. Fultz, J.W. Cahn, J.R. Manning, J.E. Morral, J.A. Simmons (Eds.), Mathematics of Microstructural Evolution, The Minerals, Metals & Materials Society, Warrendale, PA, 1996, pp. 15–22.
[15] H. Telley, T.M. Liebling, A. Mocellin, Phil. Mag. B73 (1996) 395–408.
[16] H. Telley, T.M. Liebling, A. Mocellin, Phil. Mag. B73 (1996) 409–427.
[17] J. Geiger, A. Roósz, P. Barkóczy, Acta Mater. 49 (2001) 623–629.
[18] L.-Q. Chen, W. Yang, Phys. Rev. B 50 (1994) 15752–15756.
[19] I. Steinbach, F. Pezzolla, B. Nestler, M. Seeßelberg, R. Prieler, G.J. Schmitz, Physica D 94 (1996) 135–147.
[20] D. Fan, L.Q. Chen, Acta Mater. 45 (1997) 611–632.
[21] D. Fan, C. Geng, L.Q. Chen, Acta Mater. 45 (1997) 1115–1126.
[22] M.T. Lusk, Proc. R. Soc. Lond. A 455 (1999) 677–700.
[23] R. Kobayashi, J.A. Warren, W.C. Carter, Physica D 140 (2000) 141–150.
[24] J.A. Warren, R. Kobayashi, A. Lobkovsky, W.C. Carter, Acta Mater. 51 (2003) 6035–6058.
[25] A.E. Lobkovsky, J.A. Warren, J. Cryst. Growth 225 (2001) 282–288.
[26] V. Tikare, E.A. Holm, D. Fan, L.-Q. Chen, Acta Mater. 47 (1999) 363–371.
[27] C. Maurice, in: G. Gottestein, D. Molodov (Eds.), Recrystallization and Grain Growth, vol. 1, Springer-Verlag, Berlin, 2001, pp. 123–134.
[28] M.P. Anderson, G.S. Grest, D.J. Srolovitz, Phil. Mag. B59 (1989) 293–329.
[29] J.A. Glazier, Phys. Rev. Lett. 70 (1993) 2170–2173.
[30] Y. Saito, ISIJ Int. 38 (1998) 559–566.
[31] A. Miyake, Contrib. Mineral Petrol. 130 (1998) 121–133.
[32] X.Y. Song, G.Q. Liu, Univ. Sci. Tech., Beijing 5 (1998) 129.
[33] K. Fuchizaki, T. Kusaba, K. Kawasaki, Phil. Mag. B 71 (1995) 333–357.
[34] D. Weygand, Bréchet, J. Lépinoux, W. Gust, Phil. Mag. B 79 (1999) 703–716.
[35] X. Xue, F. Righetti, H. Telley, T.M. Liebling, Phil. Mag. B 75 (1995) 576–585.
[36] E. Raabe, in: H. Weiland, B.L. Adams, A.D. Rollett (Eds.), The Minerals, Metals & Materials Society, PA, 1998, pp. 179–185.
[37] F. Wakai, N. Enomoto, H. Ogawa, Acta Mater. 48 (2000) 1297–1311.
[38] F. Wakai, J. Mater. Res. 16 (2001) 2136–2142.
[39] C.E. Krill, L.-Q. Chen, Acta Mater. 50 (2002) 3057–3073.
[40] R. Kobayashi, J.A. Warren, Physica A 356 (2005) 127–132.
[41] J.W. Cahn, J.E. Hilliard, J. Chem. Phys. 28 (1958) 258–267.
[42] S.M. Allen, J.W. Cahn, Acta Metall. 27 (1979) 1085–1095.
[43] D. Fan, L.-Q. Chen, S.-P. Chen, Mater. Sci. Eng. A 238 (1997) 78–84.
[44] N. Ma, A. Kazaryan, D.A. Dregia, Y. Wang, Acta Mater. 52 (2004) 3869–3879.
[45] Y. Suwa, Y. Saito, Mater. Trans. 46 (2005) 1208–1213.
[46] S. Sakamoto, F. Yonezawa, Kotai Butsuri (Solid State Phys.) 24 (1989) 219.
[47] Y. Suwa, Y. Saito, Mater. Trans. 46 (2005) 1214–1220.
[48] G.S. Grest, M.P. Anderson, D.J. Srolovitz, Phys. Rev. B 38 (1988) 4752–4760.
[49] K. Marthinsen, O. Hunderi, N. Ryum, Acta Mater. 44 (1996) 1681–1689.
[50] T. Nagai, K. Fuchizaki, J. Phys. Soc. Jpn. 69 (2000) 2727–2730.
[51] D.A. Aboav, Metallography 5 (1970) 251–263.
[52] D. Weaire, N. Rivier, Contemp. Phys. 25 (1984) 59–99.
[53] G. Abbruzzese, K. Lücke, Acta Metall. 34 (1986) 905–914.
[54] H. Eichelkraut, G. Abbruzzese, K. Lücke, Acta Metall. 36 (1988) 55–68.
[55] V.Y. Novikov, Acta Mater. 47 (1999) 1935–1943.
[56] F.J. Humphreys, Acta Mater. 45 (1997) 4231–4240.
[57] N. Ono, K. Kimura, T. Watanabe, Acta Mater. 47 (1999) 1007–1017.
[58] G.S. Grest, D.J. Srolovitz, M.P. Anderson, Acta Metall. 33 (1985) 509–520.
[59] A.D. Rollelt, D.J. Srolovitz, M.P. Anderson, Acta Metall. 37 (1989) 1227–1240.
[60] N.M. Hwang, B.J. Lee, C.H. Han, Scripta Mater. 37 (1997) 1761–1767.
[61] K. Mehnert, P. Klimanek, Comp. Mater. Sci. 7 (1996) 103–108.
[62] K. Mehnert, P. Klimanek, Comp. Mater. Sci. 9 (1997) 261–266.
[63] O.M. Ivasishin, S.V. Shevchenko, N.L. Vasiliev, S.L. Semiatin, Acta Mater. 51 (2003) 1019–1034.
[64] M. Miodownik, A.W. Godfrey, E.A. Holm, D.A. Hughes, Acta Mater. 47 (1999) 2661–2668.
[65] E.A. Holm, G.N. Hassold, M.A. Miodownik, Acta Mater. 49 (2001) 2981–2991.
[66] A.D. Rollett, Mater. Sci. Forum 408-4 (2002) 251–256.
[67] Y. Suwa, Y. Saito, H. Onodera, Scripta Mater. 55 (2006) 407–410.
[68] F.J. Humphreys, Scr. Metall. 27 (1992) 1557–1562.
[69] E.A. Holm, M.A. Miodownik, A.D. Rollett, Acta Mater. 51 (2003) 2701–2716.
[70] D. Weygand, Y. Bréchet, J. Lépinoux, Phil. Mag. B-80 (2000) 1987–1996.